Key Points:
- Measured magnetopause location is statistically closer to the Earth than Shue et al. (1998) modeled for storm sudden commencements (SYM-H ≥15 nT)
- When the magnetopause is compressed below 8 R_E, the average measured location is >1 R_E inside of the Shue et al. (1998) model location
- Extreme magnetopause compressions rarely reach the outer radiation belt, therefore rapid outward radial transport is required to fully explain most shadowing events

Supporting Information:
- Supporting Information S1

Correspondence to:
F. A. Staples,
frances.staples@ucl.ac.uk

Do Statistical Models Capture the Dynamics of the Magnetopause During Sudden Magnetospheric Compressions?

F. A. Staples[1] [ID], I. J. Rae[1] [ID], C. Forsyth[1] [ID], A. R. A. Smith[2] [ID], K. R. Murphy[3] [ID], K. M. Raymer[4] [ID], F. Plaschke[5] [ID], N. A. Case[6] [ID], C. J. Rodger[7] [ID], J. A. Wild[6] [ID], S. E. Milan[4] [ID], and S. M. Imber[4] [ID]

[1]Mullard Space Science Laboratory, University College London, London, UK, [2]School of GeoSciences, University of Edinburgh, Edinburgh, UK, [3]NASA Goddard Space Flight Centre, Greenbelt, MD, USA, [4]Department of Physics and Astronomy, University of Leicester, Leicester, UK, [5]Space Research Institute, Austrian Academy of Sciences, Graz, Austria, [6]Department of Physics, Lancaster University, Lancaster, UK, [7]Department of Physics, University of Otago, Dunedin, New Zealand

Abstract Under periods of strong solar wind driving, the magnetopause can become compressed, playing a significant role in draining electrons from the outer radiation belt. Also termed "magnetopause shadowing," this loss process has traditionally been attributed to a combination of magnetospheric compression and outward radial diffusion of electrons. However, the drift paths of relativistic electrons and the location of the magnetopause are usually calculated from statistical models and, as such, may not represent the time-varying nature of this highly dynamic process. In this study, we construct a database ~20,000 spacecraft crossings of the dayside magnetopause to quantify the accuracy of the commonly used Shue et al. (1998, https://doi.org/10.1029/98JA01103) model. We find that, for the majority of events (74%), the magnetopause model can be used to estimate magnetopause location to within ±1 R_E. However, if the magnetopause is compressed below 8 R_E, the observed magnetopause is greater than 1 R_E inside of the model location on average. The observed magnetopause is also significantly displaced from the model location during storm sudden commencements, when measurements are on average 6% closer to the radiation belts, with a maximum of 42%. We find that the magnetopause is rarely close enough to the outer radiation belt to cause direct magnetopause shadowing, and hence rapid outward radial transport of electrons is also required. We conclude that statistical magnetopause parameterizations may not be appropriate during dynamic compressions. We suggest that statistical models should only be used during quiescent solar wind conditions and supplemented by magnetopause observations wherever possible.

1. Introduction

Understanding the dynamics of the Van Allen radiation belts is a key challenge in understanding the terrestrial space environment. The response of the radiation belts during geomagnetic storm times is highly variable; storms may result in a net increase, a net decrease, or indeed no net response at all (Reeves et al., 2003). At any given time, a balance of acceleration and loss mechanisms could be contributing to the overall morphology of the radiation belts. It has been proposed that during storms there are repeatable phases in radiation belt response; a net loss phase where electron losses dominate, and a net acceleration phase where more electrons are accelerated than lost (Murphy et al., 2018). Furthermore, the intensity of the net loss phase of a storm can control the level of electron acceleration from the seed population in the following net acceleration phase (Bingham et al., 2018). Understanding the multiple sources of electron losses is vital to understanding radiation belt dynamics during geomagnetic storms.

There are a variety of acceleration, transport, and loss mechanisms that play a role in shaping the radiation belt environment; from gyroresonant interaction on kHz timescales through to large-scale topological changes of the magnetosphere by solar wind-magnetosphere interaction. Gyroresonant wave-particle interactions between keV "seed" electrons, injected into the inner magnetosphere during substorms, and very low frequency (VLF) whistler mode waves, act to energize radiation belt electrons to MeV energies (Baker et al., 1998; Forsyth et al., 2016; Horne & Thorne, 1998; Horne et al., 2005; Meredith et al., 2002; Summers et al., 1998). Ultralow frequency (ULF) waves transport electrons through radial diffusion (e.g., Fälthammar, 1965;

Jaynes et al., 2015) and can play a role in electron acceleration through drift-resonant wave-particle interactions (e.g., Elkington et al., 1999; Mann et al., 2013). Radial electron transport via ULF wave activity results in betatron acceleration (deceleration) of electrons as electrons are transported radially inward (outward). Even without strong ULF wave activity, electrons may still be adiabatically transported radially outward if the ring current is enhanced, and drifting electrons will adiabatically decelerate (Dessler & Karplus, 1961; McIlwain, 1966).

While outward transport and subsequent deceleration of electrons contribute to decreases in electron flux at a given energy, nonadiabatic effects account for significant and irreversible loss of electrons from the radiation belts (Kim & Chan, 1997; Li et al., 1997). Loss mechanisms act to drain the radiation belts either into interplanetary space or Earth's atmosphere. Again, gyroresonant wave-particle interaction plays an essential role by depositing electrons into the atmospheric loss cone, through pitch angle scattering processes (Gamble et al., 2008; Miyoshi et al., 2008; Rodger et al., 2015; Thorne & Kennel, 1971; Ukhorskiy et al., 2010). Localized, compressional ULF wave fields may also play a role in precipitating relativistic electrons into the atmosphere (Rae et al., 2018). Large-scale topological changes to the geomagnetic field will also result in electron loss if electron drift paths intersect the magnetopause (Green et al., 2004; Kim et al., 2008; Li et al., 1997; Saito et al., 2010). Such loss is not through precipitation into the atmosphere, but rather loss from the magnetosphere itself, known as magnetopause shadowing. The dayside magnetosphere may shrink due to compressions by enhanced solar wind dynamic pressure and/or magnetopause erosion under southward IMF (Dmitriev et al., 2014; Gosling et al., 1982; Sibeck et al., 1989). Note that in this paper we use the term compressed to synonymously refer to the inward movement of the magnetopause due to both pressure balance variations and magnetosphere erosion under southward IMF. We refer to two distinct types of magnetopause shadowing throughout this paper. When the magnetopause is suddenly compressed within the outer radiation belt on timescales similar to electron drift periods, such as during interplanetary shocks (Sibeck et al., 1989), then electron drift paths directly intersect the magnetopause. We refer to this as direct magnetopause shadowing. We distinguish "indirect" magnetopause shadowing as the combined process of outward radial diffusion toward a compressed magnetopause. Hence, during indirect magnetopause shadowing the initial particle drift path does not have to directly intersect the magnetopause boundary. Indirect magnetopause shadowing explains electron loss at comparatively low L shells where the magnetopause would never directly impact (e.g., Brautigam & Albert, 2000; Loto'Aniu et al., 2010; Miyoshi et al., 2003; Morley et al., 2010; Rodger et al., 2019; Shprits et al., 2006; Turner et al., 2012).

The relative contributions of magnetopause shadowing and precipitation throughout a geomagnetic storm are not well understood. Previous work has shown that magnetopause shadowing plays a clear role in electron flux dropout events (Morley et al., 2010; Shprits et al., 2006; Turner et al., 2012). Morley et al. (2010) studied 67 solar wind stream interface regions and showed electron flux decreased at L^* as low as 4 up to a day before the arrival of the stream interface at the bow shock. For these events, the Shue et al. (1997) magnetopause model location reached a minimum of $L = 8.5$, which is outside of where the losses were observed. Thus, Morley et al. (2010) attributed this statistical loss to combined outward radial diffusion toward a compressed magnetopause. Using the same event list, Hendry et al. (2012) analyzed precipitating electron flux measured by the Polar Operational Environmental Satellites (POES). The authors observed a large increase in precipitation following the arrival of the stream interface. During this period of high electron precipitation, Morley et al. (2010) observed a net increase in electron flux. Interestingly, Hendry et al. (2012) did not observe any increase in precipitating electron flux during the electron flux dropout itself. It therefore appears that the majority of losses prior to the stream interface arrival occur via magnetopause shadowing.

In order to understand the roles of direct or indirect shadowing on electron losses observed by Morley et al. (2010), the position of the magnetopause and the last closed drift shell (LCDS) needs to be known (Olifer et al., 2018). Both the magnetopause location and LCDS are calculated by models with a variety of underlying assumptions that are likely violated during magnetopause compressions. For example, empirical magnetopause models (e.g., Shue et al., 1997, 1998) assume that the magnetopause is in an equilibrium position, and LCDS calculations assume that the magnetospheric field can be accurately represented by global magnetic field models (e.g., Tsyganenko et al., 2003). Since we can measure the magnetopause location with relative accuracy as compared to the LCDS, we choose to focus on how well a widely used statistical magnetopause model performs, with specific reference to dynamic times. We choose to analyze the Shue et al. (1998) magnetopause model as it is widely used for radiation belt purposes (e.g., by Herrera et al., 2016;

Loto'Aniu et al., 2010; Morley et al., 2010; Murphy et al., 2015; Olifer et al., 2018; Turner et al., 2012). Previous statistical studies have shown the Shue et al. (1998) model overestimated magnetopause location by ~1 R_E at high latitudes, within the cusp region (Case & Wild, 2013). In this study we focus on the equatorial subsolar point, where the LCDS is closest to the magnetopause.

In this study we construct a multi-spacecraft database of magnetopause crossings. We use this database to investigate the dynamics of the real magnetopause for events which could lead to magnetopause shadowing, and hence radiation belt loss events (Morley et al., 2010). In order to do this, we first complete a statistical analysis of the measured magnetopause location as compared to the Shue et al. (1998) model, identifying conditions under which the measured magnetopause location is significantly different to the model, such as during interplanetary shocks and storm sudden commencements. We then show how well our statistical results hold for a case study of the 2013 St. Patrick's day storm, which is known to have a clear and well-studied radiation belt response (e.g., Albert et al., 2018; Ma et al., 2018; Olifer et al., 2018). Finally, we discuss whether a statistical correction of the Shue et al. (1998) magnetopause model is useful in determining the relative contributions of direct and indirect magnetopause shadowing during electron dropout events.

2. The Shue et al. (1998) Magnetopause Model

Shue et al. (1997) carried out a best fit of a simple parabolic function to 553 magnetopause crossings made by the ISEE 1 and 2, AMPTE/IRM, and IMP 8 satellites. This functional form depends only on the north-south component of the IMF and the solar wind dynamic pressure, D_p, which determine the subsolar standoff distance and tail flaring angle of the parabola. The measurements of the magnetopause used to fit the model were taken during solar wind conditions in the range 0.5 nPa < D_p < 8.5 nPa and IMF −18 nT < B_z < 15 nT. The authors discuss that the fitted model does not give realistic values of tail flaring angle for IMF B_z and D_p outside of these ranges. Shue et al. (1998) refitted the functional form of the Shue et al. (1997) model to include the nonlinear dependence of dynamic pressure, D_p on tail flaring angle, and also the impact of IMF B_z on subsolar standoff distance. The revised Shue et al. (1998) model gives a much improved representation of the magnetopause during values of D_p and B_z in their range of fitting data. As the Shue et al. (1998) model is easily implemented, it is extensively used to estimate magnetopause standoff distance in radiation belt physics. For brevity, we henceforth refer to this model as the "Sh98" model. The Sh98 model has frequently been applied to understanding electron flux dropout events, where magnetopause shadowing contributes to global radiation belt electron loss (Herrera et al., 2016; Loto'Aniu et al., 2010; Morley et al., 2010; Olifer et al., 2018).

It must be noted that the Sh98 model assumes a rigid parabolic magnetopause that is in equilibrium with cylindrical symmetry around the aberrated Sun-Earth line. This implies that the magnetopause responds instantaneously and globally to any changes in upstream solar wind conditions. In reality, the magnetopause is much more dynamic. For example, surface waves are driven at the magnetopause, which oscillates about its equilibrium (Plaschke, Glassmeier, Sibeck, et al., 2009). Cahill and Winckler (1992) also observed large solar wind compressions which break equilibrium and drive magnetopause oscillation. In addition, the magnetopause does not have cylindrical symmetry: Case and Wild (2013) completed a statistical comparison of the Sh98 model to a database of high-latitude Cluster magnetopause crossings, demonstrating that Sh98 model tended to overestimate the standoff distance by ~ 1 R_E near the cusps.

Shue et al. (1998) discuss the uncertainty arising from magnetopause motion. The authors calculate uncertainty as a function of IMF B_z, D_p, and solar zenith angle. The authors concluded that any deviation from the modeled average position due to, for example, magnetopause oscillations, are represented by the known Sh98 model uncertainties. Using the method described in Shue et al. (1998), Figure 1 presents how the Sh98 uncertainties vary with solar zenith angle and IMF B_z orientation, given (a) moderate (IMF $|B_z|$ and D_p of 4 nT and 2 nPa, respectively), and (b) strong (IMF $|B_z|$ and D_p of 15 nT and 8 nPa, respectively) solar wind driving. Figure 1a shows that uncertainty increases from ~0.15 R_E to 0.3 R_E for both northward and southward IMF $|B_z|$ and is ~0.025 R_E higher for southward IMF as compared to northward. The same trends of increasing uncertainty with solar zenith angle is true for higher solar wind driving (Figure 1b), but there is a larger difference between southward and northward orientated IMF, and under these conditions southward IMF now has a lower uncertainty than under northward IMF conditions. Comparing the uncertainties for southward IMF across moderate and higher solar wind driving (across Figures 1a and 1b), it is interesting to note that the uncertainty is lower for higher solar wind driving across all solar zenith angles. In contrast,
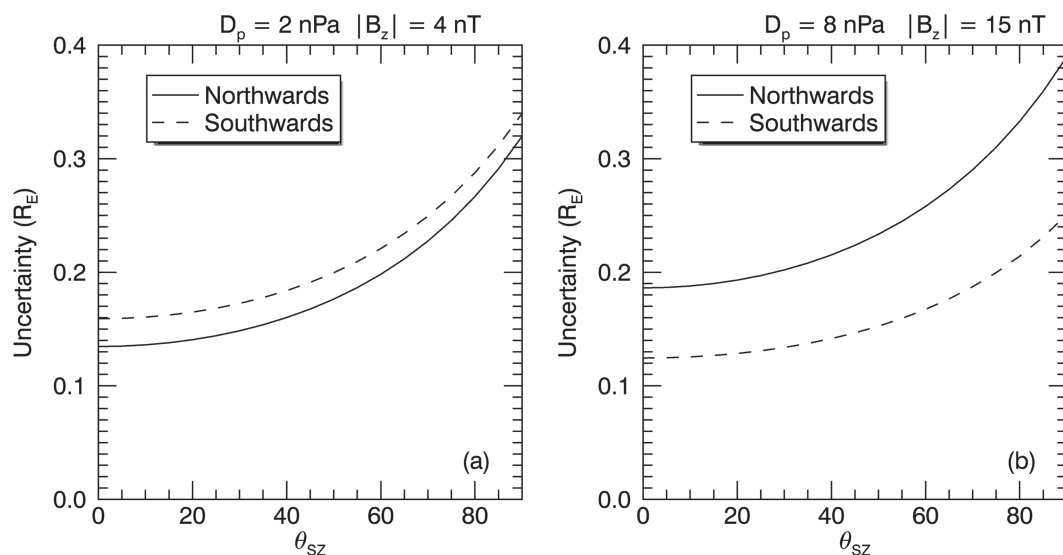
Figure 1. Uncertainty of the Shue et al. (1998) magnetopause model as a function of solar zenith angle for southward and northward orientated IMF magnitude (a) $|B_z| = 4$ nT and $D_p = 2$ nPa; (b) $|B_z| = 15$ nT and $D_p = 8$ nPa. These calculations make use of uncertainty calculation described in the original Shue et al. (1998) model paper.

for northward IMF, the uncertainties are increased. In this study, we take the maximum uncertainty in the modeled subsolar magnetopause standoff distance to be ~ 0.2 R_E, and $\lesssim 0.4$ R_E across the modeled dayside magnetopause (solar-zenith angles less than or equal to 90°, which effectively corresponds to the entirety of the dayside magnetosphere).

3. Data Set and Methodology

3.1. Building a Database of Magnetopause Observations

In order to compare the Sh98 model with measurements of the real magnetopause, we compile a database of spacecraft crossings of this boundary. When a spacecraft crosses the magnetopause, the measured magnetic field will transition between a strong, steady, and northward orientated field within the magnetosphere, and a rapidly varying magnetic field characteristic of the magnetosheath, that may be orientated in any direction. Plasma density transitions from low values in the outer magnetosphere, to higher densities in the magnetosheath where the shocked solar wind piles up and stagnates (Crooker & Siscoe, 1975).

To conduct our analysis, we have created a new database of magnetopause crossings which is further supplemented by databases from three previous studies, which are described in Table 1. These databases used automated or semi-automated classification methods. For full details of the automated algorithms and data sets we refer the reader to Plaschke, Glassmeier, Sibeck, et al. (2009); Case and Wild (2013); Raymer (2018).

To take full advantage of the THEMIS data set since its launch in 2007, we developed a semi-automated method to classify an additional 12,621 THEMIS magnetopause crossings from 2007 to 2016. Data from

Table 1
Details of Three Existing Databases of Spacecraft Magnetopause Crossings

Satellite	# crossings	Timespan	Dataset Authors
Geotail	8,548	1996–2015	Raymer (2018)
Mukai et al. (1994);			
Kokubun et al. (1994)			
THEMIS	6,697	2007	Plaschke, Glassmeier, Sibeck, et al. (2009)
Auster et al. (2008);			
McFadden et al. (2008)			
Cluster	2,688	2002–2010	Case and Wild (2013)
Balogh et al. (2001)			

THEMIS probes A, D, and E were used from 2007–2016 and THEMIS B and C from 2007–2010, after which these spacecraft were moved to lunar orbit (Angelopoulos, 2010). Only spacecraft crossings of the dayside magnetopause ($X_{GSE} > 0R_E$) were classified as this is the region electron drift paths are most likely to intersect the magnetopause.

Our approach classified magnetopause crossings from the THEMIS Flux gate magnetometer (FGM) (Auster et al., 2008) and Electrostatic Analyzer (ESA) (McFadden et al., 2008) instruments. We first created an algorithm which used a set of criteria to classify possible magnetopause crossing candidates, these crossing candidates were then manually verified on a daily basis. Data where missclassifications are clearly within the magnetosheath or magnetosphere were discarded, although a small number of missclassifications may still exist due to human error.

To create the crossing criteria we manually classified 18 magnetopause crossings by the THEMIS E probe between 17:00 and 23:00 UT on 16 June 2007. The crossing criteria were then empirically determined by optimizing the number of these crossings classified while minimizing the number of false positives. The final criteria were empirically determined as follows: When THEMIS is crossing from the magnetosphere to the magnetosheath,

1. the change in the B_z component of the magnetic field, in GSM coordinates, must be less than -0.6 nT s^{-1}, and the change in ion density must be greater than 0.08 cm^{-3} s^{-1};
2. within the magnetosphere, the average B_z component of the magnetic field must be greater than 5 nT and the average ion density must be less than 7 cm^{-3} for a 48 s interval;
3. the first two crossing criteria must be met within a 60 s interval.

If THEMIS is crossing from the magnetosheath to the magnetosphere, we reverse the first criteria. To prevent spurious measurements from high-frequency noise when calculating the first criteria, we downsampled measurements of the B$_z$ component of FGM measurements from a 3 s resolution to 24 s and ESA measurements of ion density ware reduced from 3 to 36 s resolution. Once these crossings were visually verified, the database contained 34,428 confirmed magnetopause crossings. We have removed multiple crossings of the magnetopause that occurred within 10 min, retaining only the innermost crossing for each probe. The innermost crossing was used so that our database is comparable to the Sh98 model, which used only the innermost crossing in a series of crossings to fit the model. Removing multiple crossings reduced the database to 12,621 crossings.

The Plaschke, Glassmeier, Sibeck, et al. (2009) magnetopause database also contains a large number of multiple magnetopause crossings due to the nature of their study of magnetopause oscillations. Multiple crossings within 10 min are also removed from this database, retaining only the innermost crossing for each probe. Finally, we cross referenced the Plaschke, Glassmeier, Sibeck, et al. (2009) database with our THEMIS database to ensure THEMIS crossings are not double counted. As before, the innermost crossing of the magnetopause from either database within a 10 min interval was retained. This reduces the Plaschke, Glassmeier, Sibeck, et al. (2009) database to 1,910 crossings and the database we classified for this study is reduced to 11,821 crossings.

This renders a final database of 24,967 THEMIS, Cluster, and Geotail magnetopause crossings spanning almost two solar cycles from 1996–2016. Figure 2 shows the spatial distribution of magnetopause crossings over all solar zenith angles for $2 \times 2\ R_E$ bins. Figure 2 shows the number of crossings on the dayside magnetopause, with the maximum number of crossings in any bin is 1,892 crossings between 8 to 10 $R_E\ X_{GSM}$ and 0 to $-2\ R_E\ Z_{GSM}$ (panel c). The lowest number of magnetopause crossings occur on the magnetopause tail ($X_{GSM} < 0\ R_E$ in Figures 2a and 2c) where many spatial bins only contain a single crossing. The coverage of the down-tail magnetopause is significantly less than the dayside since these crossings are taken only from the Geotail database. Note, in the following analysis, we take all magnetopause measurements from the dayside magnetopause only (from 06–18 MLT) since our main focus is to investigate the role of magnetopause shadowing on the radiation belts. This reduces our database to a total of 19,973 measurements of the dayside magnetopause, which we use to perform our statistical analysis for the remainder of this study.

We use solar wind data provided by the NASA/Goddard Space Flight Centers OMNI data set through Coordinated Data Analysis Web (CDAWeb; https://omniweb.gsfc.nasa.gov/) that comprises solar wind measurements from the ACE, Wind, IMP 8, and Geotail missions. The solar wind data are propagated to the
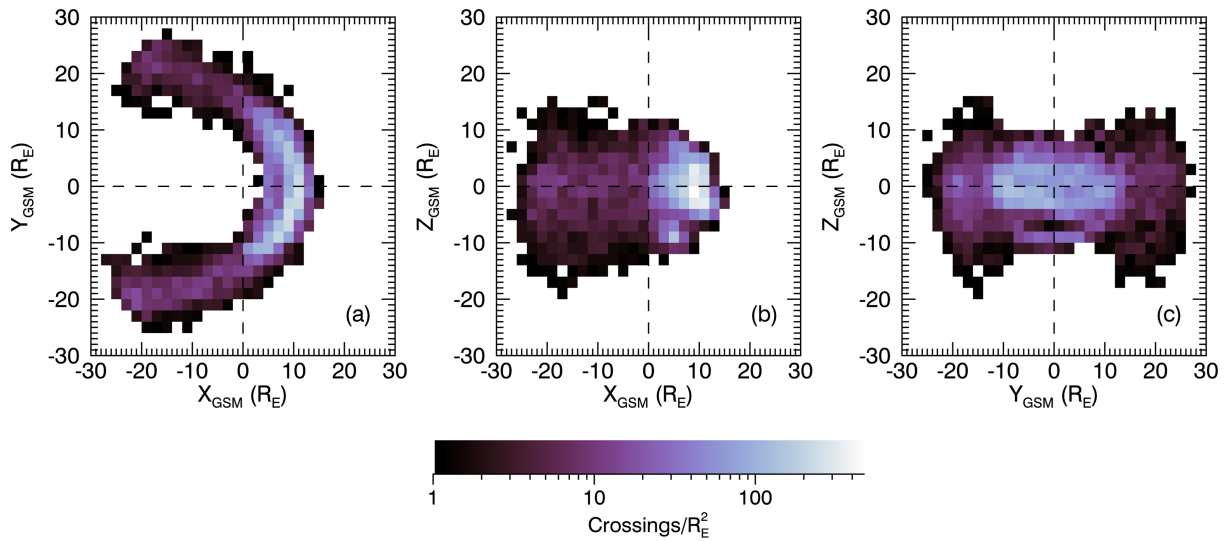
Figure 2. 2-D histogram of magnetopause crossings in the (a) X_{GSM}-Y_{GSM} plane; (b) Y_{GSM}-Z_{GSM} plane; (c) X_{GSM}-Z_{GSM} plane.

bow shock nose and has a temporal resolution of 5 min. It is expected that propagation time from the bow shock to the magnetopause is similar to this 5 min resolution (Villante et al., 2004).

We also use the Symmetric Horizontal (SYM-H) index at a 5 min resolution, as the de facto high-resolution version of the Dst index (Wanliss & Showalter, 2006). The SYM-H index is calculated in a similar manner to Dst by ground based, midlatitude magnetometer stations. These data are also provided in the OMNI data set.

3.2. Comparing Magnetopause Observations to a Modeled Location

We define ΔR as the radial distance between the measured location of a spacecraft magnetopause crossing, R_{SC}, and the distance to the abberated Sh98 model magnetopause, R_{Mod}, for the same solar zenith angle of the spacecraft, such that $\Delta R = R_{Mod} - R_{SC}$. If $\Delta R > 0$ then the model overestimates the magnetopause location; that is, the Sh98 magnetopause is located at a larger radial distance than the measured magnetopause. Conversely, if $\Delta R < 0$ then the Sh98 model underestimates the magnetopause location; that is, the Sh98 model is closer to the Earth than the measurement. Finally, if $\Delta R = 0$ to within an uncertainty of ± 0.4 R_E, then we conclude that the model and the measurement agree.

It is also important to estimate the position of the subsolar magnetopause where an electron drift path is more likely to intersect the magnetopause. By assuming that the functional shape of the Sh98 magnetopause is correct (i.e., that the shape and flaring angle, α, is correct) then we can project spacecraft measurements from any dayside magnetopause crossing to the abberated subsolar point, $R_{0_{SC}}$, by rearranging the Sh98 functional form (Plaschke, Glassmeier, Auster, et al., 2009; Plaschke, Glassmeier, Sibeck, et al., 2009);

$$R_{0_{SC}} = R_{SC} \left(\frac{2}{1 + \cos\theta} \right)^{-\alpha} \tag{1}$$

where θ is the solar zenith angle of the spacecraft crossing position, calculated by taking the inverse cosine of the dot product between the aberrated Sun-Earth line and the position vector of the spacecraft in GSE coordinates. We then define the difference between the modeled subsolar standoff distance and the measured equivalent subsolar standoff distance as $\Delta R_0 = R_{0_{Mod}} - R_{0_{SC}}$, where $R_{0_{Mod}}$ is the modeled subsolar standoff distance.

Finally, we also define the percentage change in distance to be $\Delta R/R_{SC}$ to normalize for times where there is a compressed or expanded magnetopause, and in order to compare crossings across all dayside solar zenith angles to each other.

4. Results

4.1. Statistical Evaluation of Magnetopause Location

The distributions of ΔR and ΔR_0 are shown in Figure 3a and 3b, respectively. Figure 3a shows ΔR to not be normally distributed as the mean and median values are not equal; the mean $\Delta R = 0.13$ R_E and the median
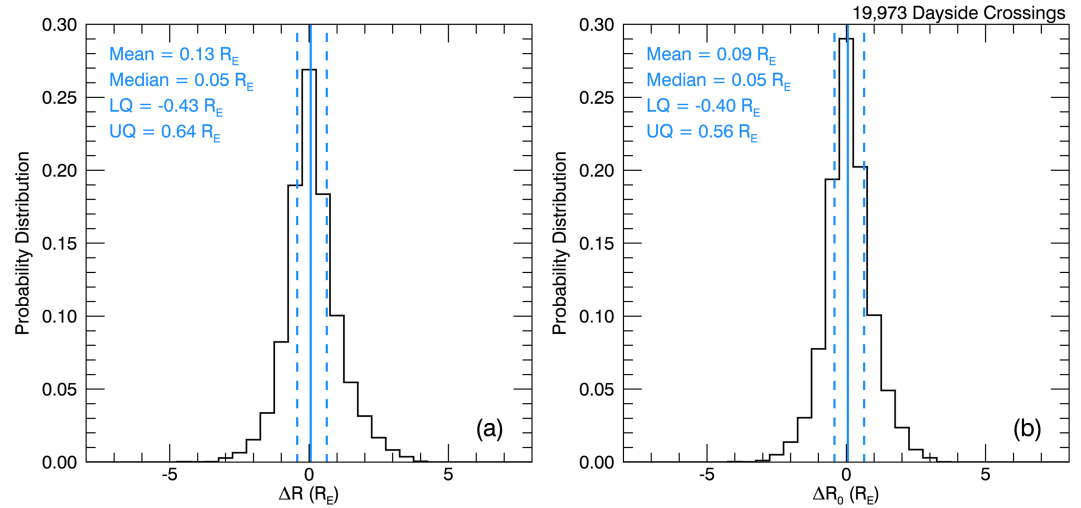
Figure 3. (a) The distribution of ΔR for measurements of the dayside magnetopause. (b) The distribution of ΔR_0 for measurements of the dayside magnetopause. The solid blue line shows the median value for each panel and the dotted blue lines show the interquartile range.

$\Delta R = 0.05 \, R_E$. This asymmetry implies that there are a higher number of instances where the measured magnetopause is closer to Earth than the modeled distance. Furthermore, 74% of measurements lie within 1 standard deviation of the mean, which in this case is 0.97 R_E. The upper and lower quartiles of ΔR are $-0.43 \, R_E$ and 0.64 R_E, respectively. The difference between the median and the mean is less than the Sh98 model uncertainty of $\pm 0.4 \, R_E$, but there is a large spread in ΔR, with only 40% of measurements being within $\leq 0.4 \, R_E$.

Figure 3b shows that ΔR_0 is also not a normal distribution as the mean and median values are not equal; with a mean $\Delta R_0 = 0.09 \, R_E$ and median $\Delta R_0 = 0.05 \, R_E$. Furthermore, 70 % of measurements occur within a standard deviation of the mean, where $\sigma = \pm 0.84 \, R_E$. The upper and lower quartiles of ΔR_0 are $= -0.40 \, R_E$ to 0.56 R_E, respectively. The difference between the median and the mean is less than the Sh98 model uncertainty of $\pm 0.2 \, R_E$ (Figure 1), but there is a large spread in ΔR_0, with only 24% of measurements being within $\leq 0.2 \, R_E$.

To see how ΔR varies for different measured standoff distances, in Figure 4 we investigate the median magnetopause distance calculated by the Sh98 model, R_{Mod}, as a function of experimentally observed magnetopause distance, R_{SC}. We note this figure describes spacecraft crossings at all measured solar zenith angles, R_{SC}, rather than equivalent subsolar standoff, R_0. The shaded area shown in the figure indicates the interquartile range of R_{SC} measurements. Within the shaded region, it can be seen that the distribution is closest to the line of unity, so median $R_{Mod} \simeq R_{SC}$, indicating that the Sh98 model is accurately calculating magnetopause standoff distance at locations between 10.6 and 12 R_E. However, there is clearly a different gradient than unity. A multiple linear regression to the distribution of median R_{Mod} is given by the purple line in Figure 4. We find that the experimentally measured magnetopause distance as a function of median modeled magnetopause distance is best described by $R_{SC} = \frac{R_{Mod} - 3.68}{0.68}$.

In order to assess whether different solar wind conditions are influencing the underestimation and overestimation of magnetopause location by the Sh98 model, we examine distributions of $\Delta R / R_{SC}$ for varying solar wind dynamic pressure and north-south IMF. These figures are included in the supporting information Figures S1 and S2, respectively. While there was
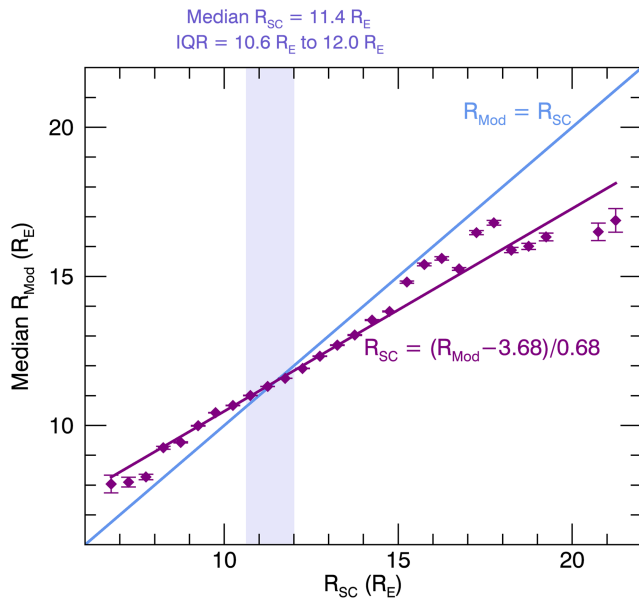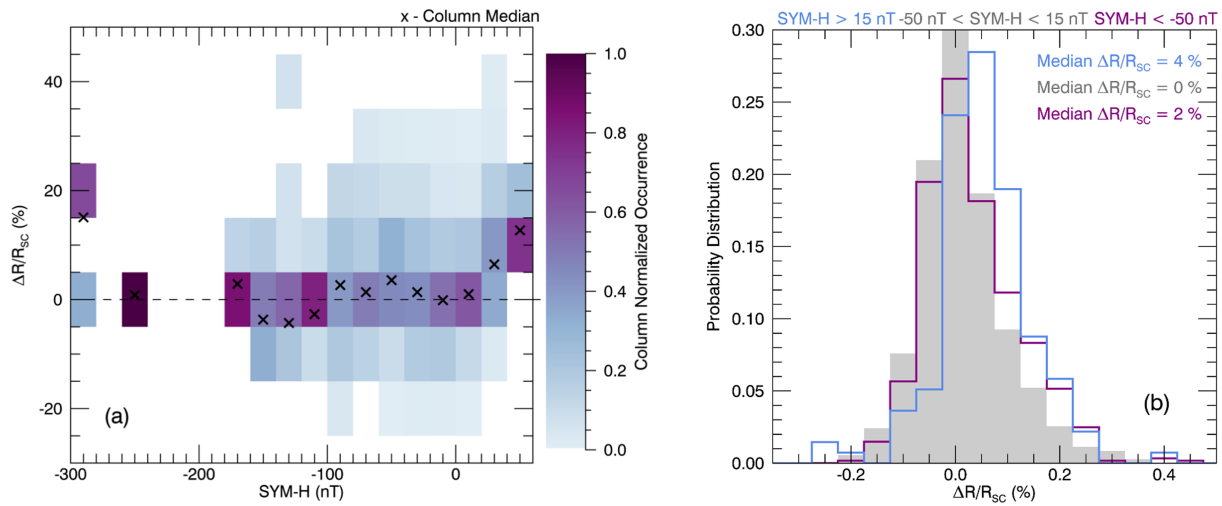

Figure 4. Purple diamonds show the median standoff distance calculated by the Shue et al. (1998) model, R_{Mod}, corresponding to spacecraft magnetopause crossing measured at a given standoff distance, R_{SC}. The error bars show the propagated error of the Shue et al. (1998) model (see section 2). The blue line gives where $\overline{R}_{Mod} = R_{SC}$. The shaded area indicates the interquartile range (10.6 to 12.0 R_E) of observed magnetopause distance, R_{SC}.

Figure 5. (a) Column normalized distribution of percentage change in magnetopause standoff distance ($\Delta R/R_{SC}$) as a function of SYM-H. Column medians are indicated by black crosses. (b) Probability distributions of $\Delta R/R_{SC}$ separated by geomagnetic conditions; quiet times are shown by the gray histogram (-50 nT $<$ SYM-H $<$ 15 nT), storm sudden commencement phase is shown by the blue histogram (SYM-H $\geq$ 15 nT), main storm phase is shown by the purple histogram (SYM-H ≤ -50 nT).

a weak relationship between $\Delta R/R_{SC}$ and D_p, there was no evidence that strong dynamic pressures ($D_p >$ 4 nPa) are associated with large positive $\Delta R/R_{SC}$. Similarly, $\Delta R/R_{SC}$ showed a tendency to increase when IMF B_z magnitude increased, but this was not true across all B_z magnitudes.

We further examine the distribution of $\Delta R/R_{SC}$ for varying geomagnetic conditions. Figure 5a shows a 2-D histogram of $\Delta R/R_{SC}$ as a function of the SYM-H index. We column normalize the distributions, since there are many more measurements during geomagnetically quiet times (-50 nT $\lesssim$ SYM-H $\lesssim$ 15 nT) than for the rest of the distribution. Figure 5a demonstrates that the relationship between $\Delta R/R_{SC}$ and the geomagnetic conditions, as defined by SYM-H index, varies depending on phase of the geomagnetic storm. For quiet times (SYM-H between -50 and 15 nT), the maximum occurrence probabilities are peaked and centered on zero. However, for geomagnetic storm time conditions (SYM-H ≤ -50 nT), the median offset between measurement and model varies greatly between -5% to 15% for decreasing SYM-H. Moreover, for positive SYM-H, $\Delta R/R_{SC}$ has a near-constant positive offset that increases with increasingly positive SYM-H. This positive offset indicates that the magnetopause is closer to Earth than the model prediction. We note that large positive and sudden increases in SYM-H typically correspond to the storm sudden commencement phase (SSC) of a geomagnetic storm. During the SSC, SYM-H index can increase by 10s of nT on minute timescales (Dessler et al., 1960) in response to the arrival of an interplanetary shock front rapidly compressing the dayside magnetosphere. Figure 5a would therefore suggest that the magnetopause is closer to Earth by up to 15% during SSC.

To further demonstrate the observed distribution of offsets in Figure 5a between measurements and the Sh98 model observed, we examine the distribution of $\Delta R/R_{SC}$ for geomagnetically quiet times (SYM-H between -50 and 15 nT), during the main phase of geomagnetic storm (SYM-H ≤ -50 nT) and for storm sudden commencement (SYM-H $\geq$ 15 nT), shown in Figure 5b. There are 19,140 measurements of $\Delta R/R_{SC}$ for SYM-H between -50 and 15 nT. This distribution is peaked at $\Delta R/R_{SC} = 0\%$ with upper and lower quartiles of -4% and 6%, respectively. Thus, during relatively quiet times the observed location of the magnetopause is located inside the Sh98 model location as often as it is located outside the model location. In contrast, when SYM-H ≤ -50 nT or SYM-H $\geq$ 15 nT, the peak of the distribution is positive; 2% and 4%, respectively, with upper and lower quartiles of -3% and 9% for SYM-H ≤ -50 nT and 0% and 10% for SYM-H $\geq$ 15 nT. There are 601 magnetopause measurements during SYM-H ≤ -50 nT and 137 measurements for SYM-H $\geq$ 15 nT. We use the Mann Whitney U test (Nachar, 2008) to confirm that the SSC and main storm phase distributions are statistically different as compared to the quiet time distribution, to a 95% confidence level. As such, during storm times (SYMH ≤ -50 nT) it is more likely that the magnetopause will be inside of the model location. During periods when SYMH $\geq$ 15 nT, which typically correspond to SSCs, the magnetopause location is almost exclusively inside of the model location. Thus, the magnetopause is statistically closer to
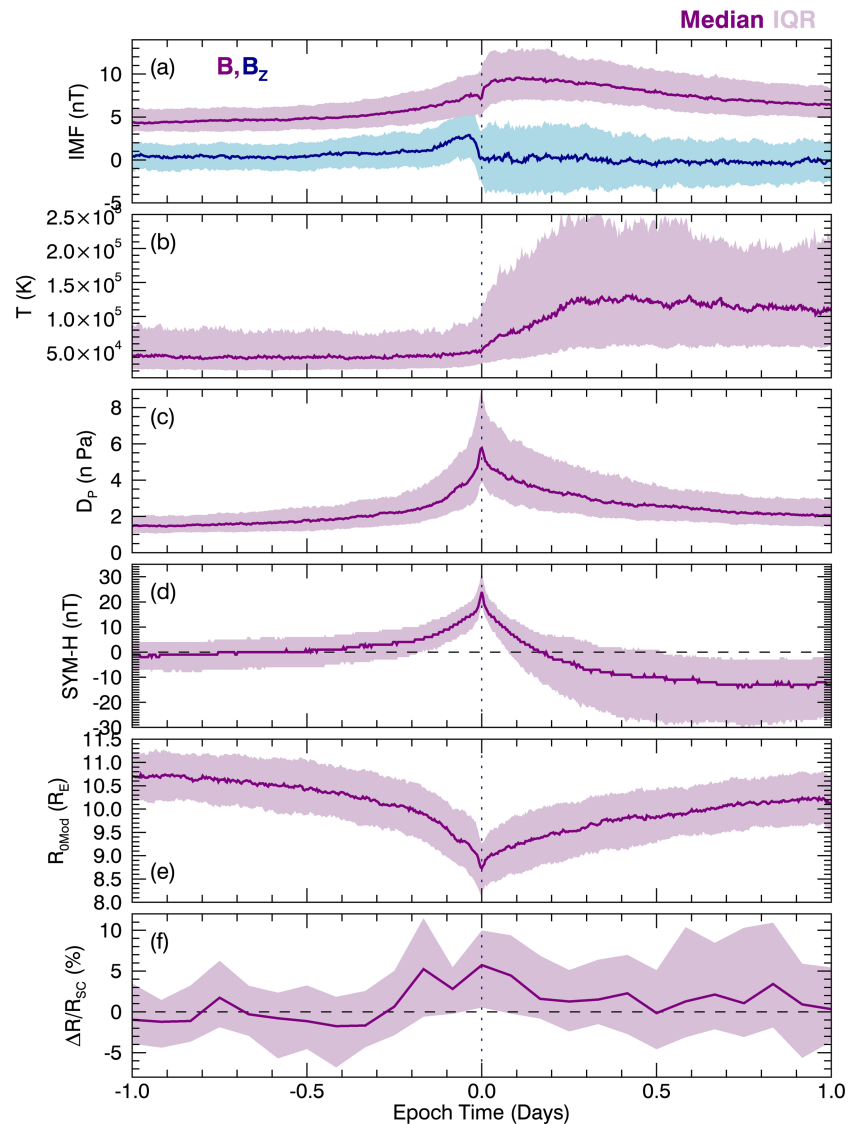
Figure 6. A superposed epoch analysis of (a) interplanetary magnetic field strength B (purple) and B_z (blue); (b) solar wind temperature, T; (c) solar wind dynamic pressure D_P; (d) SYM-H index; (e) subsolar standoff distance of the Shue et al. (1998) magnetopause model, R_{0Mod}; (f) percentage difference in radial distance between measured location of the magnetopause and the Shue et al. (1998) magnetopause model, $\Delta R/R_{SC}$. Epoch time zero is defined as the time that SYM-H reaches a peak ≥15 nT. The purple lines show median values and the interquartile range is denoted by the shaded regions. The vertical dotted line shows t_0.

the Earth than the Sh98 model during both the main phase of a geomagnetic storm and during storm sudden commencement.

To test the more extreme deviations from the Sh98 model, we perform a superposed epoch analysis (SEA) of solar wind drivers during strongly positive SYM-H conditions. We select events for this analysis where there is a peak in SYM-H which exceeds 15 nT, and where there is a spacecraft measurement of the magnetopause within a day of the peak SYM-H. Epoch time zero, t_0, is chosen as the peak value of SYM-H. We then perform the superposed epoch analysis for ± 1 day of t_0. Figure 6 shows the results of this SEA. In total there were 392 individual events used in the analysis, and 3,629 spacecraft crossings of the magnetopause across all of the epochs used. Figure 6f shows median $\Delta R/R_{SC}$ at a 2 hr resolution for the superposed epochs, whereas Figures 6a–6e have a 5 min resolution. The 2 hr resolution of Figure 6f was chosen such that the variability of $\Delta R/R_{SC}$ through the epoch analysis is clear, while maximizing the number of crossings used to calculate each median value through the epoch analysis.

Figure 6 shows strong evidence of solar wind discontinuities at t_0 characteristic of forward interplanetary shocks; a sudden increase in temperature and an increase in magnetic field strength following t_0 (Figures 6a and 6b), and a sharp peak in D_p at t_0 (Figure 6c). It is well understood that fast forward interplanetary shocks play a large role in the storm sudden commencement phase due to enhancement of magnetopause currents (e.g., Taylor, 1969). In particular empirical relationships have been derived between SSC amplitude and the change in the square root of D_p at the shock/discontinuity (Russell et al., 1992).

In response to the sudden dynamic pressure increase, the Sh98 model demonstrates a compression of the median subsolar magnetopause from $10.7\,R_E$ to $8.7\,R_E$ (Figure 6e). We observe that the SYM-H index shows a tendency to become negative following t_0 in Figure 6d. Further investigation showed that 33% of the epochs contained moderate to intense geomagnetic storms with minimum SYM-H ≤ -50 nT. A further 30% of epochs contained a minimum of SYM-H between -30 and -50 nT, indicating weak geomagnetic storms (Loewe & Prölss, 1997). This supports our suggestion that a peak in SYM-H ≥ 15 nT indicates a storm sudden commencement phase of shock-driven geomagnetic storms.

The median percentage difference between the spacecraft measurements of the magnetopause and the Sh98 model, $\Delta R/R_{SC}$, is noted to be relatively small and slowly varying between -2% and 2% until 4 hr (0.2 days) before t_0 $\Delta R/R_{SC}$ rapidly increased to 6% (Figure 6f). At the same time, the upper quartile of SYM-H exeeds 0 nT (Figure 6d). Following this rapid increase, $\Delta R/R_{SC}$ reached a maximum of 6% at t_0. Median values of $\Delta R/R_{SC}$ remain high until 2 hr (0.1 days) after t_0 and, as shown in Figure 6f, the entire interquartile range is greater than 0%, which means that in the majority of cases the Sh98 model is overestimating magnetopause distance. At times greater than 2 hr after t_0, median $\Delta R/R_{SC}$ decreases but remains positive, fluctuating between 0% and 3%, though the interquartile range is notably larger than times preceding $t_0 + 2$ hr.

It is important to comment that in Figure 5b the median $\Delta R/R_{SC}$ was calculated as 4% when we used a threshold of SYM-H ≥ 15 nT to define magnetopause measurements taken during a SSC. Whereas in the SEA presented in Figure 6f, median $\Delta R/R_{SC} = 6\%$ at t_0, which is defined as the time SYM-H peaks at a value greater than 15 nT. This difference is because the SEA of $\Delta R/R_{SC}$ has a resolution of 2 hr: Magnetopause measurements which occur within an hour of the SYM-H peak ≥ 15 nT are included in the median calculation, though SYM-H may be less than 15 nT at the time of the crossing.

4.2. Case Study: 2013 St Patrick's Day Storm

Finally, we inspect a case study of a large geomagnetic storm associated with a significant radiation belt response. The chosen event is the 2013 St. Patrick's day storm, which has both a magnetopause crossing when SYM-H > 15 nT and is a large geomagnetic storm where magnetopause shadowing should have played an important role in radiation belt electron losses. The 2013 St. Patrick's day storm has been studied extensively by the Geospace Environment Modeling (GEM) program radiation belt modeling focus group Quantitative Assessment of Radiation Belt Modeling (QARBM) as a radiation belt modeling event to quantitatively assess (e.g., Albert et al., 2018; Olifer et al., 2018; Ma et al., 2018). This event is a CME-driven geomagnetic storm in which a rapid flux dropout of the outer radiation belt precedes strong enhancements in electron flux during the geomagnetic storm (Olifer et al., 2018).

The 2013 St. Patrick's day storm has 93 individual magnetopause crossings observed by the THEMIS probes in our database between 14 and 20 March, all of which we have visually verified. From Figure 7 there are three separate solar wind pressure enhancements that lead to magnetopause variations on the 14, 15, and 17 March 2013, indicated by vertical dashed lines. We discuss each of these pressure enhancements in turn.

At around 13:00 UT on 14 March 2013, there was a small increase in D_p of up to 5 nPa (Figure 7a), which had a small corresponding SYM-H increase to 16 nT but no obvious radiation belt response (Figure 7b and 7d). The Sh98 model standoff location was compressed to $8.8\,R_E$. The equivalent standoff distance of magnetopause crossings during this compression, $R_{0_{SC}}$, agree remarkably well with the Sh98 location (Figure 7c).

Around 06:00 UT on 15 March 2013, there was a second comparatively small increase in D_p of up to 6 nPa (Figure 7a). In this case there was a clear and rapid increase in SYM-H by 20 nT, to a peak of 25 nT. There was a reduction in the ~1 MeV electron fluxes by a factor of ~10 at the outer boundary of the radiation belt, for $L > 6\,R_E$ (Figure 7d), which persisted until the major geomagnetic disturbance which began on 17 March 2013. For the 15 March pressure pulse, the Sh98 model standoff location was compressed to $8.3\,R_E$. The observed magnetopause crossings continued to agree with model values until the magnetopause was maximally compressed at 07:00 UT. Immediately following this maximum compression on 15 March there
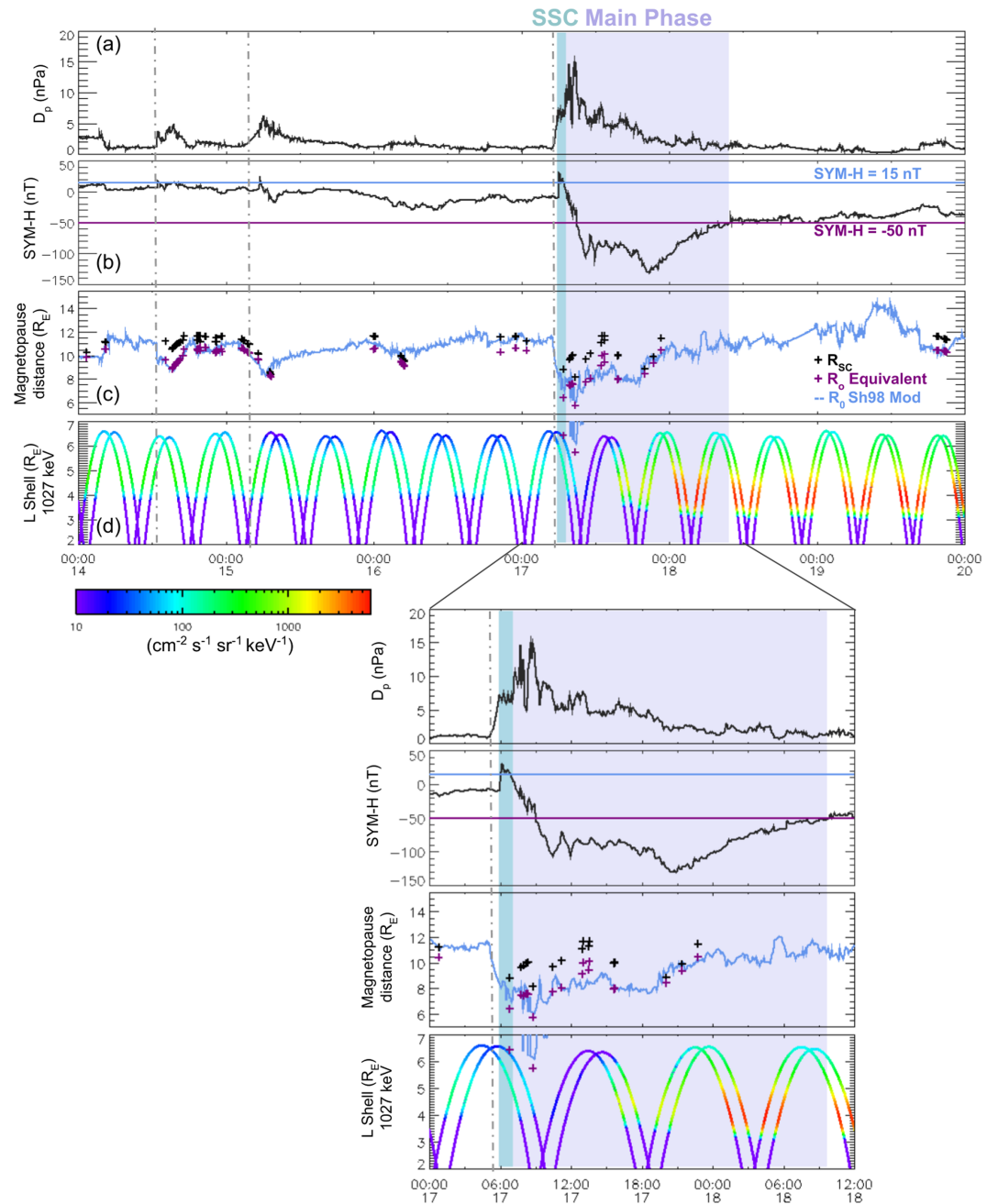
Figure 7. March 2013 St. Patrick's day storm case study from 14–20 March 2013; (a) solar wind dynamic pressure, D_p; (b) SYM-H index, with the blue and purple horizontal lines denoting SYM-H = −15 and −50 nT, respectively; (c) the subsolar standoff distance of the Sh98 model in blue, black crosses denoting magnetopause crossing distance at any solar zenith angle, and purple crosses denoting equivalent standoff distance of those magnetopause crossings, $R_{0_{SC}}$; (d) ~1 MeV electron flux from the Van Allen Probes A and B MagEIS instruments to illustrate radiation belt activity. Vertical dashed lines indicate pressure enhancements. Blue- and purple-shaded areas denote the SSC and main phase of the geomagnetic storm respectively. A zoomed-in plot of panels (a)–(d) during the geomagnetic storm on 17 March is also shown.

are two magnetopause crossings where the observed magnetopause is 0.9 R_E and 1.2 R_E (10% and 15%) closer to the radiation belts than the Sh98 model distance.

On 17 March 2013, the CME arrival was accompanied by a sudden increase in D_p from 1 to 15 nPa. The SYM-H index responded accordingly, with a sharp increase to 31 nT, before the main phase of the storm where SYM-H decreased down to −131 nT. During the main phase of the storm, the ∼1 MeV electron fluxes decreased by around 2 orders of magnitude, a reduction that persisted for 7 hr. Enhancements resulting from the storm dominated over the losses on 18 March 2013; on this day the ∼1 MeV electron fluxes increased by 3 orders of magnitude and the radial peak in flux moved to lower L of ∼4 R_E. The Sh98 model standoff location (R_{Mod}) was compressed in response to the pressure enhancement, and was as close to the Earth as 6.1 R_E during the main phase of the storm. At 08:45 UT, where the Sh98 model output was at its minimum standoff distance, the subsolar projection of an observed THEMIS E magnetopause crossing was 5.7 R_E, which is 0.4 R_E (7%) closer to Earth than the Sh98 model calculation of 6.1 R_E. During the storm sudden commencement, there was one crossing of the magnetopause made by THEMIS D at 06:48 UT, with an equivalent subsolar standoff distance of 6.4 R_E. At this time, the Sh98 model was calculated as 7.3 R_E, a difference of 0.9 R_E (or 14%) closer to Earth than the model calculation. Equivalent subsolar standoff measurements during the main phase of the storm were perhaps even more variable, ranging between 5.7 and 10 R_E, indicating that the Sh98 model does not reflect the true magnetopause location during this highly disturbed time. Taking the model uncertainty as ∼0.2 R_E at the subsolar point (following the calculations presented in Figure 1), only 15% of measurements on 17 March 2013 were within this error. The Sh98 model underestimated standoff distance by >0.2 R_E for 40% of measurements, and overestimated standoff distance by >0.2 R_E for 45% of measurements.

5. Discussion and Conclusions

The ability to accurately calculate the magnetopause standoff distance is integral to the process of modeling and prediction of trapped electron fluxes in the outer radiation belt. An accurate magnetopause location is central to accurately determining whether radiation belt losses will occur via direct magnetopause shadowing, indirect magnetopause shadowing, or not at all.

Olifer et al. (2018) studied a series of geomagnetic storms, where a model magnetopause and last closed drift shell (LCDS) could be determined. These authors also used the Shue et al. (1998) magnetopause model and concluded that there was a strong correspondence between the variation in the LCDS and measured electron fluxes during these case studies. Olifer et al. (2018) concluded that their results implied that indirect magnetopause shadowing, that is, outward radial transport combined with enhanced ULF wave radial diffusion, played a key role in relativistic losses during rapid flux dropout events. Albert et al. (2018) investigated the behaviors of different LCDS models, finding that models of the LCDS differ distinctly in L^* depending on the assumptions used, the different magnetic field model inputs, and calculation procedures. Interestingly, Olifer et al. (2018) calculated that the Sh98 magnetopause model was, at times, earthward of the LCDS prior to SSC (see lower panel of Figure 3, Olifer et al., 2018). That the LCDS can lie outside of the Sh98 model location exemplifies that LCDS models should be used with caution. Matsumura et al. (2011) used an empirical outer boundary of the radiation belt as a proxy for the last closed drift shell. These authors found that this empirical boundary is well correlated with the magnetopause standoff distance as calculated by Shue et al. (1997) during loss events, when the outer boundary of the radiation belt moved earthward in conjunction with a compression of the Shue et al. (1997) model. Given that we are unable to measure the LCDS, but we can measure the magnetopause location, we have tested the validity of the most common magnetopause model used for radiation belt physics.

In this study, we constructed an empirical database of ∼20,000 spacecraft crossings of the dayside magnetopause. We compared the locations of each crossing with the predicted Sh98 model location given the prevailing solar wind conditions, provided by the OMNI database. The radial difference between the measured and predicted magnetopause location was distributed about zero, with upper and lower quartiles of ∼ −0.5 R_E and 0.6 R_E, respectively, for all dayside locations (Figure 3a) and when mapped to the subsolar point (Figure 3b). However, the distributions were slightly skewed toward positive values for both ΔR and ΔR_0 as the means of both distributions were ∼0.1 R_E with a standard deviation of ∼1 R_E. This means that the Sh98 model accurately represented the magnetopause location to within ∼1 R_E, on average. Figure 7 corroborates this finding, as the Sh98 model and the measured magnetopause are in agreement during the

14 and 15 March 2013 time period. It must be noted that the calculation of $R_{0_{SC}}$ and ΔR_0 assumes that the shape of the Sh98 model, specifically the level of tail flaring, α, is correct. If a spacecraft crossing is at a large solar zenith angle (i.e., not near the magnetopause nose) this method of mapping to the subsolar point may introduce error in $R_{0_{SC}}$ or ΔR_0 calculations if α is inaccurate.

Further, while we found that the predicted Sh98 model magnetopause location was accurate to within $\sim$1 R_E of the observed magnetopause locations between 10.5 R_E and 12 R_E, the uncertainty increased for more extreme cases, that is, when the measured magnetopause location was outside of this range (Figure 4). On average, the Sh98 model underestimated standoff distance for crossings measured at distances >12 R_E, and overestimated standoff distance for crossings measured at distances <10.6 R_E. We applied a multiple linear regression to the observed and average modelled values and found that across all prevailing conditions between 1996–2016, the relations can be described by a linear function $R_{SC} = \frac{R_{Mod}-3.68}{0.68}$. This fit of the model to our crossing database may suggest that a simple correction made to the Sh98 location would better reflect the *average* measured location. However, we emphasize that the linear regression shown in Figure 4 should not be used to correct the Sh98 model on an event by event basis without careful consideration. This is particularly important for values of R_{Mod} smaller than those used in the linear regression ($R_{Mod} < 7.4R_E$), where the prediction of R_{SC} for the linear regression becomes unrealistically small. For example, for a modeled prediction of 6.6 R_E, the linear regression would imply that the magnetopause position would be 3.9 R_E.

Discrepancies between measurements and the model for large observed magnetopause distances ($R_{SC} > 12.0\,R_E$) could be due, in part, to inaccuracies in the paraboloid Sh98 model shape, that is, the magnetopause is closer than the model near the nose, and further away near the flanks, which would be suggestive of a more flared magnetotail. Further inaccuracies in the paraboloid Sh98 model shape may arise from the no-axisymmetric shape of the magnetopause, that is, dawn-dusk asymmetries (Haaland et al., 2017) and indentations due to the magnetospheric cusp regions (Case & Wild, 2013). We also considered whether the difference between measurements and the model for small observed magnetopause distances ($R_{SC} < 10.6$ R_E) could be due to the Sh98 inaccurately representing the influence of dynamic pressure or IMF on the magnetopause location (Supporting Information S1 and S2, respectively). While dynamic pressure and IMF do not appear to be responsible for systematic discrepancies between measured magnetopause location and the Sh98 model, we would recommend that the Sh98 model should only be used in the range of 0.5 nPa $< D_p < 8$ nPa and -15 nT $< B_z < 10$ nT. This is based on the distribution of median $\Delta R/R_{SC}$ measurements in Figures S1 and S2, respectively, and the range of dynamic pressures and IMF magnitudes for which Shue et al. (1998) had magnetopause measurements to fit the Sh98 model (Section 2). Finally, we note that the observed discrepancy between model and measurements may be, in part, due to rapid solar wind fluctuations. Processes such as solar wind fluctuations would mean that the magnetopause location is not in equilibrium, as assumed by the Sh98 model. In this study we have shown that during dynamic times such as interplanetary shocks, an average location will not reflect the true magnetopause location. Hence, any empirical relationship should therefore be used with extreme caution.

We have shown that the distance between the measured magnetopause and the modeled location varies for different geomagnetic conditions (Figure 5). We highlight that, for increasingly positive SYM-H, the magnetopause location is increasingly overestimated by the Sh98 model. This overestimate may be up to a maximum median of 13% between 40 nT $\leq$ SYM-H $\leq$ 60 nT and maximum single event value of 42% at a SYM-H of 18 nT (Figure 5a). We identify these periods of positive SYM-H as the SSC phase (Figure 6). Hence, for increasingly large SSCs, the magnetopause location can be expected to be significantly closer to the Earth than previously thought. Figure 6 shows a SEA of solar wind drivers during strongly positive SYM-H conditions associated with SSCs. We find that the driver of strong positive increases of magnetopause compressions show characteristics of fast forward shocks. The strong positive increases in SYM-H were found to be associated with magnetospheric compressions (Figure 6e). At the maximum SYM-H, the magnetosphere was maximally compressed and observations of the magnetopause were overestimated by 6% on average by the Sh98 magnetopause model (Figure 6f).

Solar wind pressure pulses and fast forward shocks have been known to have an associated radiation belt response (e.g., Hietala et al., 2014; Kilpua et al., 2019; Sibeck et al., 1989), which is usually attributed to shock-driven ULF waves which radially diffuse electrons toward the magnetopause (e.g., Claudepierre et al., 2010). In particular, relativistic electron flux in the outer radiation belt has been observed to drop out in response to a stream interface of high-speed solar wind streams; Morley et al. (2010) showed results
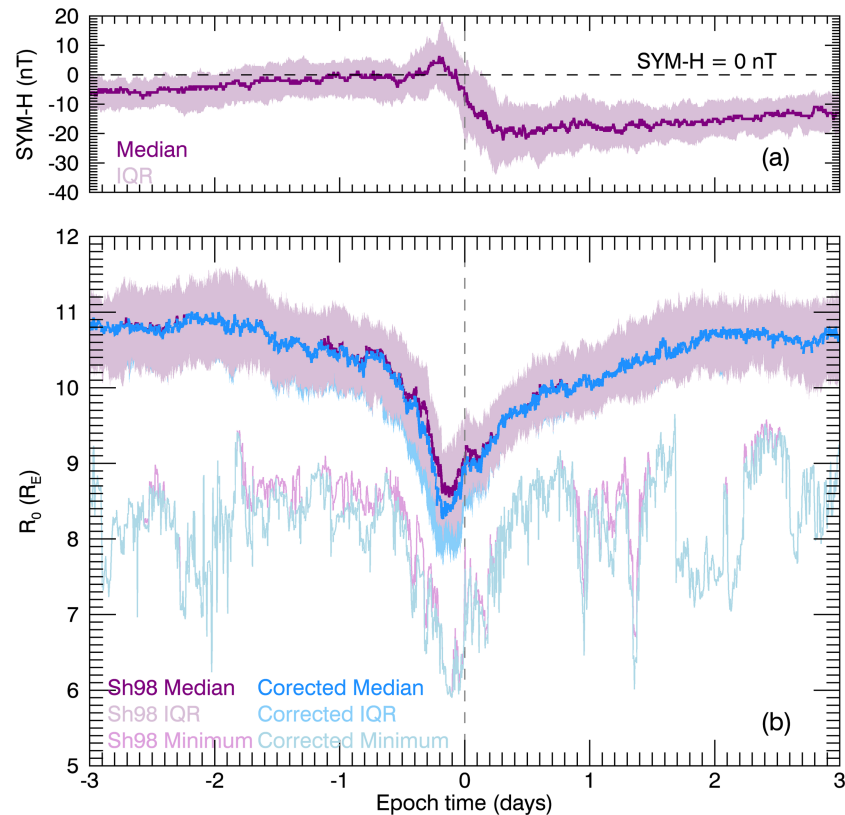
Figure 8. Superposed epoch analysis of 67 high-speed solar wind stream interface events identified by Morley et al. (2010). (a) The dark purple line shows median SYM-H index and the light purple-shaded region shows the interquartile range; (b) The dark purple line shows the median Shue et al. (1998) subsolar standoff distance of the magnetopause, R_{Mod}, the light purple-shaded area shows the interquartile range and the light pink line shows the minimum standoff distance of R_{Mod} at a given epoch time. The dark blue line shows the median corrected magnetopause standoff distance, the shaded blue area shows the interquartile range, and the light blue line shows the minimum standoff distance of R_{Cor}. The correction factor is based on variations in $\Delta R / R_{\text{SC}}$ associated with a peak in SYM-H index (Figure 6 (f)).

of a SEA where electron flux drops out at L^* as low as 4.5 in response to high-speed solar wind stream interface regions. The authors observed that the magnetopause standoff distance becomes compressed to 8.5 R_{E} and concluded that electron losses occurred by more indirect magnetopause shadowing, that is, magnetopause compression and rapid outward radial transport. The results we have presented in Figure 6 for fast forward shocks, such as high-speed solar wind stream interfaces, would suggest that it is highly likely that the magnetopause is compressed significantly closer to the outer radiation belt than the Sh98 model calculates. In Figure 8 we investigate using a correction to the Sh98 magnetopause model for the 67 stream interface events identified by Morley et al. (2010). For each individual epoch, we identify the maximum value of SYM-H. Then, for ±12 hr (0.5 day) from this peak in SYM-H, we increase or decrease the Sh98 standoff distance by a factor that is time-dependent according to the $\Delta R / R_{\text{SC}}$ results shown in Figure 6f, for example, for $t_0 + 5$ hr of a SYM-H peak, R_{Mod} is decreased by 5%. Figure 8a shows a SEA of SYM-H during the SI events and Figure 8b shows a SEA of the Sh98 subsolar magnetopause standoff (pink-purple colors) and corrected magnetopause standoff distances are shown by blue colors.

Figure 8 shows a SEA of R_{Mod} (pink-purple colors) and R_{Cor} is shown by blue colors. In addition to the interquartile range of the Sh98 modeled magnetopause position during the SIs, which reached a minimum of 8 R_{E}, the full range of values was as low as 6 R_{E}. Given that the Sh98 model standoff distances had values within geostationary orbit (6.6 R_{E}) we find that, at least in some circumstances, that direct magnetopause shadowing may occur following a number of these SIs. Moreover, when we apply a correction to the modeled standoff distance, we find that the estimated median magnetopause location is compressed to 8.2 R_{E}, with a lower quartile value of 7.6 R_{E}, and the minimum magnetopause compression during all the epochs was 5.9 R_{E}. If a median magnetopause location is used then direct magnetopause shadowing would not

be predicted, regardless of whether a correction is applied to the Sh98 model or not. However, direct magnetopause shadowing may still occur during more extreme conditions, particularly during the SSC period. Figure 8 illustrated that, under more extreme or variable conditions, this standoff distance can be significantly closer to the Earth than the Sh98 model. Given that our maximum difference between measurement and model is 42% closer to the Earth during positive SYM-H, this would lead to the magnetopause being well inside geostationary orbit and as close as 5 R_E. We suggest that this may happen during dynamic periods such as SSC but that, during the main and recovery phase of storms, it is more likely that outward radial diffusion must still be invoked to explain electron losses i.e., via indirect magnetopause shadowing.

In order to investigate the time-dependent accuracy of model magnetopause motion during a radiation belt dropout event, we studied the 2013 St Patrick's day storm. We found that, during more quiescent times before the geomagnetic storm, the observed and model magnetopause locations are very similar between 14 and 16 March 2013. However, at the end of the 16 and 17 March 2013 the Sh98 model magnetopause standoff distance was rarely accurate compared to observed magnetopause crossings. Of the observed magnetopause standoff distances 85% were either greater than (40%) or less than (45%) the Sh98 magnetopause standoff by distance greater than the model uncertainty. From our measurements of the magnetopause we calculated the equivalent dayside magnetopause to reach a minimum of 5.7 R_E, 0.4 R_E closer to the outer radiation belt than the Sh98 calculation. In Figure 7d, we observed that this compression of the magnetopause will have been capable of causing direct shadowing of the outer radiation belt. Indirect shadowing will also have played a role in this dropout event as ULF wave power was high during this period (Ma et al., 2018), transporting electrons at lower L shells toward the compressed magnetopause. Betatron deceleration of electrons as they are transported radially outward could further contribute toward the apparent decrease in electron flux of a given energy channel. The combined result was that the entire outer radiation belt decreased in flux by 2 orders of magnitude.

We now discuss several additional aspects concerning how our analysis might be affected by both small-scale transitory structures in the magnetopause and by large-scale motion of the magnetopause. First, models such as the Sh98 model aim to characterize the global shape and location of the magnetopause, but in reality the magnetopause contains smaller scale structures. For example, Kelvin-Helmholtz waves occur at the magnetopause flanks due to an instability created by a velocity shear at the magnetopause boundary layer (e.g., Hasegawa et al., 2004; Pu & Kivelson, 1983). Hot flow anomalies in the solar wind are known to decrease pressure in regions of the magnetosheath for short periods of time (~7 min) allowing the magnetopause to bulge outward by up to 5 R_E near the hot flow anomaly core (Archer et al., 2014; Jacobsen et al., 2009; Sibeck et al., 1999). Conversely, fast magnetosheath jets can produce local magnetopause indentations of up to ~1–2 R_E depth if a jet penetrates to the magnetopause (Amata et al., 2011; Hietala et al., 2014; Plaschke et al., 2016; Shue et al., 2009). Surface waves on the magnetopause have also been observed as a result of impinging magnetosheath jets (Amata et al., 2011; Plaschke, Glassmeier, Sibeck, et al., 2009). If a magnetopause crossing takes place in a location where the magnetopause is locally perturbed, then the crossing may not represent the global magnetopause location, if such a function exists. Not only do these structures add uncertainty to the estimation of magnetopause location, they potentially have effects on the dynamics of magnetospheric plasma. Both Kelvin-Helmholtz waves and magnetospheric jets are known drivers of ULF waves (Archer et al., 2013; Chen & Hasegawa, 1974; Claudepierre et al., 2008; Hughes, 1994; Southwood, 1974), which act to diffuse magnetospheric plasma. Earthward perturbations of the magnetopause due to a fast magnetosheath jet near the subsolar point may intersect radiation belt electron drift paths. What is more, local magnetopause compressions due to fast magnetosheath jets only occur for tens of seconds up to 3 min (Archer et al. 2012). If a magnetosheath jet is sustained for minute timescales near the subsolar magnetopause, it could certainly contribute toward a substantial loss of the ultrarelativistic electron population, which have drift periods of ~5 min. However, electron losses in the outer radiation belt have not yet been observed directly in connection with magnetosheath jets (Plaschke et al., 1983). We expect more global changes in magnetopause location to largely govern total radiation belt dropout events as most of the relativistic electron population have drift orbits longer than the timescale of a magnetosheath jet.

Second, in our analysis we use only the innermost of a sequence of magnetopause crossings to represent the position of the magnetopause at that time. Measured magnetopause crossings will primarily be due to the magnetopause passing over a quasi-stationary spacecraft, and hence the minimum magnetopause location will lie somewhere inside the spacecraft location. In part, this is addressed by the Shue et al. (1998) model, whereby the innermost magnetopause crossing was taken to be the minimum standoff distance in

their model. However, during a large compression by an interplanetary shock, or local compression due to a fast magnetosheath jet, this would not reflect the minimum magnetopause location. Moreover, any interplanetary shock that leads to an SSC will set the magnetopause in motion until it reaches an equilibrium position, and so an average magnetopause correction is not necessarily representative of specific event behavior (Freeman et al., 1995). Freeman et al. (1995) studied magnetopause motion during time varying solar wind conditions, such as those studied in this paper. The authors found that, to a first-order approximation, the magnetopause behaves like a 2-D elastic membrane and exhibits oscillation of a damped harmonic oscillator in response to changes in solar wind dynamic pressure. In their idealized system, the magnetopause oscillation is highly damped with a natural eigenperiod of ∼7 min. Hence, it is certainly possible that electrons with drift periods of ∼5 min could intersect the oscillating magnetopause location when the magnetopause is undergoing this damped harmonic motion before settling to a more equilibrium position. This would involve the total loss of ultrarelativistic electrons but only a small disturbance to the medium energy radiation belt electron population - much like the reports of ultrarelativistic electron losses currently attributed to EMIC wave-driven precipitation (e.g., Aseev et al., 2017; Shprits et al., 2017).

Ideally, continuous observations of the magnetopause location would elucidate the time-dependent response of the magnetopause to variable solar wind driving and geomagnetic storms. These observations could be conducted by the Solar Wind-Magnetosphere-Ionosphere Link Explorer, or "SMILE," a small class science mission which is under development between the European Space Agency and Chinese Academy of Sciences (Raab et al., 2016). This novel experiment will use observations of soft X-ray emissions from charge exchange interactions in the Earth's magnetosheath, from which a three-dimensional magnetopause location can be inferred. The SMILE mission provides a unique opportunity to investigate the role of the global magnetopause on radiation belt dynamics.

5.1. Summary:

- During periods of slowly varying solar wind conditions and quiescent geomagnetic activity, we have found that the Sh98 magnetopause model is a good estimate of magnetopause location within ± 1 $R_{\rm E}$.
- We highlight that the time-dependent response of the magnetopause to fast changes is solar wind conditions (e.g., interplanetary shocks) cannot be captured by a statistical magnetopause model such as the Shue et al. (1998) model. During such times, other parameterizations of the magnetopause location should be considered, supplemented by measurements of the magnetopause wherever possible.
- The time-dependent nature of the magnetopause must be taken into account for any realistic description of radiation belt electron losses through the magnetopause. In particular, we show that a new parameterization may be critical when quantifying electron flux dropouts in the radiation belts, particularly at very high energies.

References

Albert, J., Selesnick, R., Morley, S., Henderson, M., & Kellerman, A. (2018). Calculation of last closed drift shells for the 2013 gem radiation belt challenge events. *Journal of Geophysical Research: Space Physics*, *123*, 9597–9611. https://doi.org/10.1029/2018JA025991

Amata, E., Savin, S., Ambrosino, D., Bogdanova, Y., Marcucci, M., Romanov, S., & Skalsky, A. (2011). High kinetic energy density jets in the earths magnetosheath: A case study. *Planetary and Space Science*, *59*(7), 482–494. https://doi.org/10.1016/j.pss.2010.07.021

Angelopoulos, V. (2010). The artemis mission, *The artemis mission* (pp. 3–25). New York, NY: Springer. https://doi.org/10.1007/978-1-4614-9554-3_2

Archer, M., Hartinger, M., & Horbury, T. (2013). Magnetospheric magic frequencies as magnetopause surface eigenmodes. *Geophysical Research Letters*, *40*, 5003–5008. https://doi.org/10.1002/grl.50979

Archer, M., Turner, D., Eastwood, J., Horbury, T., & Schwartz, S. (2014). The role of pressure gradients in driving sunward magnetosheath flows and magnetopause motion. *Journal of Geophysical Research: Space Physics*, *119*, 8117–8125. https://doi.org/10.1002/2014JA020342

Aseev, N., Shprits, Y., Drozdov, A., Kellerman, A., Usanova, M., Wang, D., & Zhelavskaya, I. (2017). Signatures of ultrarelativistic electron loss in the heart of the outer radiation belt measured by van allen probes. *Journal of Geophysical Research: Space Physics*, *122*, 10–102. https://doi.org/10.1002/2017JA024485

Auster, H., Glassmeier, K., Magnes, W., Aydogar, O., Baumjohann, W., Constantinescu, D., et al. (2008). The themis fluxgate magnetometer. *Space Science Reviews*, *141*(1-4), 235–264. https://doi.org/10.1007/s11214-008-9365-9

Baker, D., Li, X., Blake, J., & Kanekal, S. (1998). Strong electron acceleration in the earth's magnetosphere. *Advances in Space Research*, *21*(4), 609–613. https://doi.org/10.1016/S0273-1177(97)00970-8

Balogh, A., Carr, C. M., Acuna, M., Dunlop, M., Beek, T., Brown, P., et al. (2001). The cluster magnetic field investigation: overview of in-flight performance and initial results. *Annales Geophysicae*, *19*, 1207–1217. https://hal.archives-ouvertes.fr/hal-00316910

Bingham, S., Mouikis, C., Kistler, L., Boyd, A., Paulson, K., Farrugia, C., et al. (2018). The outer radiation belt response to the storm time development of seed electrons and chorus wave activity during cme and cir driven storms. *Journal of Geophysical Research: Space Physics*, *123*, 10–139. https://doi.org/10.1029/2018JA025963

Brautigam, D., & Albert, J. (2000). Radial diffusion analysis of outer radiation belt electrons during the october 9, 1990, magnetic storm. *Journal of Geophysical Research*, *105*(A1), 291–309. https://doi.org/10.1029/1999JA900344

Cahill, L., & Winckler, J. (1992). Periodic magnetopause oscillations observed with the goes satellites on march 24, 1991. *Journal of Geophysical Research*, *97*(A6), 8239–8243. https://doi.org/10.1029/92JA00433

Case, N., & Wild, J. (2013). The location of the earth's magnetopause: A comparison of modeled position and in situ cluster data. *Journal of Geophysical Research: Space Physics*, *118*, 6127–6135. https://doi.org/10.1002/jgra.50572

Chen, L., & Hasegawa, A. (1974). A theory of long-period magnetic pulsations: 2. impulse excitation of surface eigenmode. *Journal of Geophysical Research*, *79*(7), 1033–1037. https://doi.org/10.1029/JA079i007p01033

Claudepierre, S., Elkington, S., & Wiltberger, M. (2008). Solar wind driving of magnetospheric ulf waves: Pulsations driven by velocity shear at the magnetopause. *Journal of Geophysical Research*, *113*, A05218. https://doi.org/10.1029/2007JA012890

Claudepierre, S., Hudson, M., Lotko, W., Lyon, J., & Denton, R. (2010). Solar wind driving of magnetospheric ulf waves: Field line resonances driven by dynamic pressure fluctuations. *Journal of Geophysical Research*, *115*, A11202. https://doi.org/10.1029/2010JA015399

Crooker, N. U., & Siscoe, G. L. (1975). Subsonic magnetosheath observations from explorer 33. *Journal of Geophysical Research*, *80*(31), 4368–4371. https://doi.org/10.1029/JA080i031p04368

Dessler, A., Francis, W., & Parker, E. (1960). Geomagnetic storm sudden-commencement rise times. *Journal of Geophysical Research*, *65*(9), 2715–2719. https://doi.org/10.1029/JZ065i009p02715

Dessler, A., & Karplus, R. (1961). Some effects of diamagnetic ring currents on van allen radiation. *Journal of Geophysical Research*, *66*(8), 2289–2295. https://doi.org/10.1029/JZ066i008p02289

Dmitriev, A., Suvorova, A., Chao, J.-K., Wang, C., Rastaetter, L., Panasyuk, M., et al. (2014). Anomalous dynamics of the extremely compressed magnetosphere during 21 january 2005 magnetic storm. *Journal of Geophysical Research: Space Physics*, *119*, 877–896. https://doi.org/10.1002/2013JA019534

Elkington, S. R., Hudson, M. K., & Chan, A. A. (1999). Acceleration of relativistic electrons via drift-resonant interaction with toroidal-mode pc-5 ulf oscillations. *Geophysical Research Letters*, *26*(21), 3273–3276. https://doi.org/10.1029/1999GL003659

Fälthammar, C.-G. (1965). Effects of time-dependent electric fields on geomagnetically trapped radiation. *Journal of Geophysical Research*, *70*(11), 2503–2516. https://doi.org/10.1029/JZ070i011p02503

Forsyth, C., Rae, I., Murphy, K., Freeman, M., Huang, C.-L., Spence, H., et al. (2016). What effect do substorms have on the content of the radiation belts? *Journal of Geophysical Research: Space Physics*, *121*, 6292–6306. https://doi.org/10.1002/2016JA022620

Freeman, M., Freeman, N., & Farrugia, C. (1995). A linear perturbation analysis of magnetopause motion in the newton-busemann limit. *Annales Geophysicae*, *13*, 907–918. https://doi.org/10.1007/s00585-995-0907-0

Gamble, R. J., Rodger, C. J., Clilverd, M. A., Sauvaud, J.-A., Thomson, N. R., Stewart, S., et al. (2008). Radiation belt electron precipitation by man-made vlf transmissions. *Journal of Geophysical Research*, *113*, A10211. https://doi.org/10.1029/2008JA013369

Gosling, J., Asbridge, J., Bame, S., Feldman, W., Paschmann, G., Sckopke, N., & Russell, C. (1982). Evidence for quasi-stationary reconnection at the dayside magnetopause. *Journal of Geophysical Research*, *87*(A4), 2147–2158. https://doi.org/10.1029/JA087iA04p02147

Green, J., Onsager, T., O'Brien, T., & Baker, D. (2004). Testing loss mechanisms capable of rapidly depleting relativistic electron flux in the earth's outer radiation belt. *Journal of Geophysical Research*, *109*, A12211. https://doi.org/10.1029/2004JA010579

Haaland, S., Hasegawa, H., De Keyser, J., & Maes, L. (2017). Dawn-dusk asymmetries at the terrestrial magnetopause: Observations. *Dawn-Dusk Asymmetries in Planetary Plasma Environments*, *230*, 73. https://doi.org/10.1002/9781119216346.ch6

Hasegawa, H., Fujimoto, M., Phan, T.-D., Reme, H., Balogh, A., Dunlop, M., et al. (2004). Transport of solar wind into earth's magnetosphere through rolled-up kelvin–helmholtz vortices. *Nature*, *430*(7001), 755. https://doi.org/10.1038/nature02799

Hendry, A. T., Rodger, C. J., Clilverd, M. A., Thomson, N. R., Morley, S. K., & Raita, T. (2012). Rapid radiation belt losses occurring during high-speed solar wind stream-driven storms: Importance of energetic electron precipitation. *Dynamics of the Earths Radiation Belts and Inner Magnetosphere*, *199*, 213–223. https://doi.org/10.1029/2012GM001299

Herrera, D., Maget, V., & Sicard-Piet, A. (2016). Characterizing magnetopause shadowing effects in the outer electron radiation belt during geomagnetic storms. *Journal of Geophysical Research: Space Physics*, *121*, 9517–9530. https://doi.org/10.1002/2016JA022825

Hietala, H., Kilpua, E., Turner, D., & Angelopoulos, V. (2014). Depleting effects of icme-driven sheath regions on the outer electron radiation belt. *Geophysical Research Letters*, *41*, 2258–2265. https://doi.org/10.1002/2014GL059551

Horne, R. B., & Thorne, R. M. (1998). Potential waves for relativistic electron scattering and stochastic acceleration during magnetic storms. *Geophysical Research Letters*, *25*(15), 3011–3014. https://doi.org/10.1029/98GL01002

Horne, R. B., Thorne, R. M., Shprits, Y. Y., Meredith, N. P., Glauert, S. A., Smith, A. J., et al. (2005). Wave acceleration of electrons in the van allen radiation belts. *Nature*, *437*(7056), 227. https://doi.org/10.1038/nature03939

Hughes, WJeffrey (1994). Magnetospheric ulf waves: A tutorial with a historical perspective. *Solar Wind Sources of Magnetospheric Ultra-Low-Frequency Waves*, *81*, 1–11. https://doi.org/10.1029/GM081p0001

Jacobsen, K., Phan, T., Eastwood, J., Sibeck, D., Moen, J., Angelopoulos, V., et al. (2009). Themis observations of extreme magnetopause motion caused by a hot flow anomaly. *Journal of Geophysical Research*, *114*, A08210. https://doi.org/10.1029/2008JA013873

Jaynes, A., Baker, D., Singer, H., Rodriguez, J., Loto'aniu, T., Ali, A., et al. (2015). Source and seed populations for relativistic electrons: Their roles in radiation belt changes. *Journal of Geophysical Research: Space Physics*, *120*, 7240–7254. https://doi.org/10.1002/2015JA021234

Kilpua, E., Turner, D., Jaynes, A., Hietala, H., Koskinen, H., Osmane, A., et al. (2019). Outer van allen radiation belt response to interacting interplanetary coronal mass ejections. *Journal of Geophysical Research: Space Physics*, *124*, 1927–1947. https://doi.org/10.1029/2018JA026238

Kim, H.-J., & Chan, A. A. (1997). Fully adiabatic changes in storm time relativistic electron fluxes. *Journal of Geophysical Research*, *102*(A10), 22,107–22,116. https://doi.org/10.1029/97JA01814

Kim, K. C., Lee, D.-Y., Kim, H.-J., Lyons, L. R., Lee, E., Öztürk, M. K., & Choi, C. (2008). Numerical calculations of relativistic electron drift loss effect. *Journal of Geophysical Research*, *113*, A09212. https://doi.org/10.1029/2007JA013011

Kokubun, S., Yamamoto, T., Acuña, M. H., Hayashi, K., Shiokawa, K., & Kawano, H. (1994). The geotail magnetic field experiment. *Journal of Geomagnetism and Geoelectricity*, *46*(1), 7–22. https://doi.org/10.5636/jgg.46.7

Li, X., Baker, D., Temerin, M., Cayton, T., Reeves, E., Christensen, R., et al. (1997). Multisatellite observations of the outer zone electron variation during the november 3–4, 1993, magnetic storm. *Journal of Geophysical Research*, *102*(A7), 14,123–14,140. https://doi.org/10.1029/97JA01101

Loewe, C., & Prölss, G. (1997). Classification and mean behavior of magnetic storms. *Journal of Geophysical Research*, *102*(A7), 14,209–14,213. https://doi.org/10.1029/96JA04020

Loto'Aniu, T., Singer, H., Waters, C., Angelopoulos, V., Mann, I., Elkington, S., & Bonnell, J. (2010). Relativistic electron loss due to ultralow frequency waves and enhanced outward radial diffusion. *Journal of Geophysical Research*, *115*, A12245. https://doi.org/10.1029/2010JA015755

Ma, Q., Li, W., Bortnik, J., Thorne, R., Chu, X., Ozeke, L., et al. (2018). Quantitative evaluation of radial diffusion and local acceleration processes during gem challenge events. *Journal of Geophysical Research: Space Physics*, *123*, 1938–1952. https://doi.org/10.1002/2017JA025114

Mann, I. R., Lee, E., Claudepierre, S., Fennell, J. F., Degeling, A., Rae, I., et al. (2013). Discovery of the action of a geophysical synchrotron in the earths van allen radiation belts. *Nature Communications*, *4*, 2795. https://doi.org/10.1038/ncomms3795

Matsumura, C., Miyoshi, Y., Seki, K., Saito, S., Angelopoulos, V., & Koller, J. (2011). Outer radiation belt boundary location relative to the magnetopause: Implications for magnetopause shadowing. *Journal of Geophysical Research*, *116*, A06212. https://doi.org/10.1029/2011JA016575

McFadden, J., Carlson, C., Larson, D., Ludlam, M., Abiad, R., Elliott, B., et al. (2008). The themis esa plasma instrument and in-flight calibration. *Space Science Reviews*, *141*(1-4), 277–302. https://doi.org/10.1007/s11214-008-9440-2

McIlwain, C. E. (1966). Ring current effects on trapped particles. *Journal of Geophysical Research*, *71*(15), 3623–3628. https://doi.org/10.1029/JZ071i015p03623

Meredith, N. P., Horne, R. B., Iles, R. H., Thorne, R. M., Heynderickx, D., & Anderson, R. R. (2002). Outer zone relativistic electron acceleration associated with substorm-enhanced whistler mode chorus. *Journal of Geophysical Research*, *107*(A7), 1144. https://doi.org/10.1029/2001JA900146

Miyoshi, Y., Morioka, A., Misawa, H., Obara, T., Nagai, T., & Kasahara, Y. (2003). Rebuilding process of the outer radiation belt during the 3 november 1993 magnetic storm: Noaa and exos-d observations. *Journal of Geophysical Research*, *108*(A1), 1004. https://doi.org/10.1029/2001JA007542

Miyoshi, Y., Sakaguchi, K., Shiokawa, K., Evans, D., Albert, J., Connors, M., & Jordanova, V. (2008). Precipitation of radiation belt electrons by emic waves, observed from ground and space. *Geophysical Research Letters*, *35*, L23101. https://doi.org/10.1029/2008GL035727

Morley, S. K., Friedel, R. H., Spanswick, E. L., Reeves, G. D., Steinberg, J. T., Koller, J., et al. (2010). Dropouts of the outer electron radiation belt in response to solar wind stream interfaces: Global positioning system observations. *Proceedings of the Royal Society A: Mathematical, Physical and Engineering Sciences*, *466*(2123), 3329–3350. https://doi.org/10.1098/rspa.2010.0078

Mukai, T., Machida, S., Saito, Y., Hirahara, M., Terasawa, T., Kaya, N., et al. (1994). The low energy particle (LEP) experiment onboard the geotail satellite. *Journal of Geomagnetism and Geoelectricity*, *46*(8), 669–692. https://doi.org/10.5636/jgg.46.669

Murphy, K. R., Mann, I. R., & Sibeck, D. G. (2015). On the dependence of storm time ulf wave power on magnetopause location: Impacts for ulf wave radial diffusion. *Geophysical Research Letters*, *42*, 9676–9684. https://doi.org/10.1002/2015GL066592

Murphy, K. R., Watt, C., Mann, I. R., Jonathan Rae, I., Sibeck, D. G., Boyd, A., et al. (2018). The global statistical response of the outer radiation belt during geomagnetic storms. *Geophysical Research Letters*, *45*, 3783–3792. https://doi.org/10.1002/2017GL076674

Nachar, N. (2008). The mann-whitney u: A test for assessing whether two independent samples come from the same distribution. *Tutorials in Quantitative Methods for Psychology*, *4*(1), 13–20. https://doi.org/10.20982/tqmp.04.1.p013

Olifer, L., Mann, I. R., Morley, S. K., Ozeke, L. G., & Choi, D. (2018). On the role of last closed drift shell dynamics in driving fast losses and van allen radiation belt extinction. *Journal of Geophysical Research: Space Physics*, *123*, 3692–3703. https://doi.org/10.1029/2018JA025190

Plaschke, F., Glassmeier, K., Auster, H., Constantinescu, O., Magnes, W., Angelopoulos, V., et al. (2009). Standing alfvén waves at the magnetopause. *Geophysical Research Letters*, *36*, L02104. https://doi.org/10.1029/2008GL036411

Plaschke, F., Glassmeier, K., Sibeck, D., Auster, H., Constantinescu, O., Angelopoulos, V., & Magnes, W. (2009). Magnetopause surface oscillation frequencies at different solar wind conditions. *Annales Geophysicae: Atmospheres, Hydrospheres and Space Sciences*, *27*, 4521. https://doi.org/10.5194/angeo-27-4521-2009

Plaschke, F., Hietala, H., Angelopoulos, V., & Nakamura, R. (2016). Geoeffective jets impacting the magnetopause are very common. *Journal of Geophysical Research: Space Physics*, *121*, 3240–3253. https://doi.org/10.1002/2016JA022534

Plaschke, F., Hietala, H., Archer, M., Blancos-Cano, X., Kajdič, P., Karlsson, T., Lee, S. H., Omidi, N., Palmroth, M., Roytershteyn, V., Schmid, D., Sergeev, V., & Sibeck, D. (2018). Jets downstream of collisionless shocks. *Space Science Reviews*, *214*(5).https://doi.org/10.1007/s11214-018-0516-3

Pu, Z.-Y., & Kivelson, M. G. (1983). Kelvin: Helmholtz instability at the magnetopause: Solution for compressible plasmas. *Journal of Geophysical Research*, *88*(A2), 841–852. https://doi.org/10.1029/JA088iA02p00841

Raab, W., Branduardi-Raymont, G., Wang, C. H., Dai, L., Donovan, E. F., Enno, G. A., et al. (2016). Smile: a joint esa/cas mission to investigate the interaction between the solar wind and earth's magnetosphere. In *Astronomical telescopes + instrumentation*, Proc. SPIE (pp. 990,502). https://doi.org/10.1117/12.2231984

Rae, I. J., Murphy, K. R., Watt, C. E., Halford, A. J., Mann, I. R., Ozeke, L. G., et al. (2018). The role of localized compressional ultra-low frequency waves in energetic electron precipitation. *Journal of Geophysical Research: Space Physics*, *123*, 1900–1914. https://doi.org/10.1002/2017JA024674

Raymer, K. M. (2018). *Influences on the location of the earths magnetopause*. Leicester, UK: University of Leicester, Department of Physics and Astronomy. http://hdl.handle.net/2381/43064

Reeves, G., McAdams, K., Friedel, R., & O'Brien, T. (2003). Acceleration and loss of relativistic electrons during geomagnetic storms. *Geophysical Research Letters*, *30*(10), 1529. https://doi.org/10.1029/2002GL016513

Rodger, C. J., Hendry, A. T., Clilverd, M. A., Kletzing, C. A., Brundell, J. B., & Reeves, G. D. (2015). High-resolution in situ observations of electron precipitation-causing emic waves. *Geophysical Research Letters*, *42*, 9633–9641. https://doi.org/10.1002/2015GL066581

Rodger, C. J., Turner, D. L., Clilverd, M. A., & Hendry, A. T. (2019). Magnetic local time-resolved examination of radiation belt dynamics during high speed solar wind speed-triggered substorm clusters. *Geophysical Research Letters*, *46*, 10,219–10,229. https://doi.org/10.1029/2019GL083712

Russell, C., Ginskey, M., Petrinec, S., & Le, G. (1992). The effect of solar wind dynamic pressure changes on low and mid-latitude magnetic records. *Geophysical Research Letters*, *19*(12), 1227–1230. https://doi.org/10.1029/92GL01161

Saito, S., Miyoshi, Y., & Seki, K. (2010). A split in the outer radiation belt by magnetopause shadowing: Test particle simulations. *Journal of Geophysical Research*, *115*, A08210. https://doi.org/10.1029/2009JA014738

Shprits, Y. Y., Kellerman, A., Aseev, N., Drozdov, A. Y., & Michaelis, I. (2017). Multi-mev electron loss in the heart of the radiation belts. *Geophysical Research Letters*, *44*, 1204–1209. https://doi.org/10.1002/2016GL072258

Shprits, Y., Thorne, R., Friedel, R., Reeves, G., Fennell, J., Baker, D., & Kanekal, S. (2006). Outward radial diffusion driven by losses at magnetopause. *Journal of Geophysical Research*, *111*, A11214. https://doi.org/10.1029/2006JA011657

Shue, J.-H., Chao, J., Fu, H., Russell, C., Song, P., Khurana, K., & Singer, H. (1997). A new functional form to study the solar wind control of the magnetopause size and shape. *Journal of Geophysical Research*, *102*(A5), 9497–9511. https://doi.org/10.1029/97JA00196

Shue, J.-H., Chao, J.-K., Song, P., McFadden, J., Suvorova, A., Angelopoulos, 1V, et al. (2009). Anomalous magnetosheath flows and distorted subsolar magnetopause for radial interplanetary magnetic fields. *Geophysical Research Letters*, *36*, L18112. https://doi.org/10.1029/2009GL039842

Shue, J.-H., Song, P., Russell, C., Steinberg, J., Chao, J., Zastenker, G., et al. (1998). Magnetopause location under extreme solar wind conditions. *Journal of Geophysical Research*, *103*(A8), 17,691–17,700. https://doi.org/10.1029/98JA01103

Sibeck, D., Baumjohann, W., Elphic, R., Fairfield, D., Fennell, J., Gail, W., et al. (1989). The magnetospheric response to 8-minute period strong-amplitude upstream pressure variations. *Journal of Geophysical Research*, *94*(A3), 2505–2519. https://doi.org/10.1029/JA094iA03p02505

Sibeck, D., Borodkova, N., Schwartz, S., Owen, C., Kessel, R., Kokubun, S., et al. (1999). Comprehensive study of the magnetospheric response to a hot flow anomaly. *Journal of Geophysical Research*, *104*(A3), 4577–4593. https://doi.org/10.1029/1998JA900021

Southwood, D. (1974). Some features of field line resonances in the magnetosphere. *Planetary and Space Science*, *22*(3), 483–491. https://doi.org/10.1016/0032-0633(74)90078-6

Summers, D., Thorne, R. M., & Xiao, F. (1998). Relativistic theory of wave-particle resonant diffusion with application to electron acceleration in the magnetosphere. *Journal of Geophysical Research*, *103*(A9), 20,487–20,500. https://doi.org/10.1029/98JA01740

Taylor, H. E. (1969). Sudden commencement associated discontinuities in the interplanetary magnetic field observed by imp 3. *Solar Physics*, *6*(2), 320–334. https://doi.org/10.1007/BF00150957

Thorne, RMi, & Kennel, C. (1971). Relativistic electron precipitation during magnetic storm main phase. *Journal of Geophysical research*, *76*(19), 4446–4453. https://doi.org/10.1029/JA076i019p04446

Tsyganenko, N., Singer, H., & Kasper, J. (2003). Storm-time distortion of the inner magnetosphere: How severe can it get? *Journal of Geophysical Research*, *108*(A5), 1209. https://doi.org/10.1029/2002JA009808

Turner, D. L., Shprits, Y., Hartinger, M., & Angelopoulos, V. (2012). Explaining sudden losses of outer radiation belt electrons during geomagnetic storms. *Nature Physics*, *8*(3), 208. https://doi.org/10.1038/nphys2185

Ukhorskiy, A., Shprits, Y., Anderson, B., Takahashi, K., & Thorne, R. (2010). Rapid scattering of radiation belt electrons by storm-time emic waves. *Geophysical Research Letters*, *37*, L09101. https://doi.org/10.1029/2010GL042906

Villante, U., Lepidi, S., Francia, P., & Bruno, T. (2004). Some aspects of the interaction of interplanetary shocks with the earth's magnetosphere: an estimate of the propagation time through the magnetosheath. *Journal of Atmospheric and Solar-Terrestrial Physics*, *66*(5), 337–341. https://doi.org/10.1016/j.jastp.2004.01.003

Wanliss, J. A., & Showalter, K. M. (2006). High-resolution global storm index: Dst versus sym-h. *Journal of Geophysical Research*, *111*, A02202. https://doi.org/10.1029/2005JA011034